ACCSCIENCE PUBLISHING

International Journal of Bioprinting

RESEARCH ARTICLE

# 3D-bioprinted active gingival hydrogel for periodontal soft tissue regeneration via TGF-β/Smad and Wnt/β-Catenin-mediated extracellular matrix remodeling

**Han Hu[1†], Yue Liao[1†], Jiachen Dong[1], Mengjun Sun[1], Xin Sun[2], Guodong Zhou[3*], and Zhongchen Song[1*]**

[1] Department of Periodontology, Shanghai Ninth People's Hospital, Shanghai Jiao Tong University School of Medicine; College of Stomatology, Shanghai Jiao Tong University; National Center for Stomatology; National Clinical Research Center for Oral Diseases; Shanghai Key Laboratory of Stomatology; Shanghai Research Institute of Stomatology, Shanghai, China

[2] Shanghai Key Laboratory of Orthopedic Implants, Department of Orthopedic Surgery, Shanghai Ninth People's Hospital, Shanghai Jiao Tong University School of Medicine, Shanghai, China

[3] Department of Stomatology, Shanghai Yangpu District Kongjiang Hospital, Shanghai, China

[†]These authors contributed equally to this work.

***Corresponding authors:**
Zhongchen Song
(szhongchen@sina.com)

Guodong Zhou
(18321801391@163.com)

**Citation:** Hu H, Liao Y, Dong J, *et al.* 3D-bioprinted active gingival hydrogel for periodontal soft tissue regeneration via TGF-β/Smad and Wnt/β-catenin-mediated extracellular matrix remodeling. *Int J Bioprint.* 2026;12(1):398-412. doi: 10.36922/IJB025430444

**Received:** October 26, 2025
**Revised:** November 28, 2025
**Accepted:** December 4, 2025
**Published online:** December 4, 2025



## Abstract

Soft tissue management is essential in periodontal, orthodontic, and implant therapies, yet autologous grafts remain limited by donor-site morbidity, inconsistent tissue quality, and restricted availability. To address these challenges, we developed an active gingival hydrogel (AGH) composed of gelatin methacrylate, chondroitin sulfate methacrylate, and gingival fibroblasts, which was fabricated into cell-laden hydrogels using extrusion-based 3D bioprinting. The AGH exhibited excellent rheological performance, print fidelity, and interconnected porous microstructures that supported nutrient diffusion and cell migration. Gingival fibroblasts cocultured with the AGH showed robust adhesion, proliferation, and collagen matrix deposition, accompanied by significant upregulation of fibronectin and type I collagen. Mechanistic studies revealed that these effects were mediated through activation of the Wnt/β-catenin and transforming growth factor-β/Smad signaling pathways, which synergistically regulate extracellular matrix remodeling and epithelial keratinization. *In vivo* experiments demonstrated that AGH implantation significantly enhanced gingival thickness, collagen density, and neovascularization while reducing inflammatory infiltration, as verified by magnetic resonance imaging as well as histological and immunohistochemical analyses. Furthermore, coculture with gingival epithelial cells promoted upregulation of *Krt10* and *Krt14*, indicating improved epithelial differentiation. Collectively, this study establishes a 3D-bioprinted active gingival hydrogel as a biomimetic and functional substitute for autologous grafts, offering a promising strategy for periodontal and peri-implant soft tissue regeneration.

***Keywords:*** Bioprinting; Gingival fibroblast; Gingival phenotype; Soft tissue augmentation; Tissue engineering

## 1. Introduction

Periodontal and peri-implant soft-tissue augmentation frequently relies on autologous connective tissue grafts, which remain the clinical gold standard for increasing gingival thickness and improving long-term stability.[1-3] However, their application is fundamentally limited by donor-site morbidity, restricted tissue availability, and postoperative discomfort.[4-6]

Beyond autologous free gingival grafts and connective tissue grafts, a variety of xenogeneic and allogeneic soft-tissue substitutes—such as acellular dermal matrices and porcine collagen matrices—have been introduced to reduce donor-site morbidity and surgical time while improving patient comfort.[7-9] These materials can increase keratinized tissue width and soft-tissue thickness around teeth and implants compared with flap procedures alone, and they are now widely used in daily practice. However, recent clinical trials and systematic reviews[3,10,11] consistently indicate that most soft-tissue substitutes still fall short of autologous grafts in the magnitude and long-term stability of keratinized tissue gain and mucosal thickening, particularly when a stable ≥2-mm band of keratinized tissue is desired. In addition, currently available substitutes are largely acellular and function as passive scaffolds, with limited ability to actively modulate extracellular matrix (ECM) remodeling or epithelial phenotype.

In this context, there is a clear need for next-generation, biology-informed constructs that combine the surgical advantages of soft-tissue substitutes with the biological performance of autologous connective tissue.

Gingival fibroblasts (GFs) play a central role in gingival phenotype maintenance and wound healing.[12] Compared with fibroblasts in nonkeratinized oral mucosa, GFs exhibit stronger ECM synthetic capacity and higher expression of collagen (COL)1, COL3, and fibronectin (FN)—molecules essential for collagen remodeling, mechanical resistance, and epithelial–mesenchymal crosstalk.[12-15] Recent studies on oral mucosal repair also highlight the importance of the Wnt/β-catenin and transforming growth factor (TGF)-β/Smad pathways in regulating fibroblast activation, ECM deposition, and keratinocyte differentiation. Wnt/β-catenin signaling promotes fibroblast migration and fibronectin transcription, whereas TGF-β/Smad is the key driver of COL1/COL3 synthesis during connective tissue maturation.[16,17] Together, these pathways contribute to the rapid, scar-resistant healing characteristic of the gingiva and provide a mechanistic basis for designing biomaterials that can actively modulate cellular behavior.

To functionally mimic the ECM microenvironment of gingival connective tissue, gelatin methacrylate (GelMA) and chondroitin sulfate methacrylate (ChsMA) are particularly suitable candidates. GelMA provides arginine-glycine-asparagine (RGD) adhesion motifs and an adjustable stiffness that resembles that of the lamina propria, supporting fibroblast attachment and elongation. ChsMA, a glycosaminoglycan-derived component, enhances hydration, viscoelasticity, and collagen synthesis while modulating inflammation.[18,19] Together, these materials can create a microenvironment favorable for fibroblast proliferation, ECM remodeling, and subsequent epithelial keratinization.

Three-dimensional (3D) bioprinting further enables the fabrication of cell-laden constructs with controlled architecture, interconnected porosity, and reproducible mechanical properties—features that conventional scaffolds cannot achieve.[20,21] By precisely arranging bioinks containing viable fibroblasts within a biomimetic matrix, bioprinting provides a promising platform for engineering living gingival-like tissue that more closely recapitulates the hierarchical structure and function of native connective tissue.

In this study, guided by single-cell transcriptomic profiling of gingival and oral mucosal fibroblasts, we designed an "active gingival hydrogel" (AGH) based on a photocrosslinkable GelMA/ChsMA matrix laden with GFs. This construct was designed to recreate a gingiva-like extracellular microenvironment, promote FN/COL1-mediated matrix remodeling, and engage Wnt/β-catenin and TGF-β/Smad signaling to support soft-tissue thickening and epithelial keratinization. The present study evaluates the printability, mechanical behavior, and biocompatibility of this construct, elucidates its underlying molecular mechanisms *in vitro*, and tests its capacity to augment gingival thickness in a rat incisor model.

This work seeks to provide a biologically active alternative to autologous grafts and to offer new insights into the design of functional substitutes for periodontal soft-tissue augmentation.

## 2. Materials and methods

### 2.1. Cell isolation and primary culture

Gingival tissue specimens containing both epithelial and connective layers were aseptically harvested from the hard palate of Sprague–Dawley rats ($n = 3$).

For GFs, fresh tissues were immediately immersed in sterile phosphate-buffered saline (PBS; Gibco, USA) supplemented with 1% penicillin–streptomycin (Gibco). Sequential enzymatic digestion was performed using collagenase IV and 0.25% trypsin–ethylenediaminetetraacetic acid (EDTA) for 60 min at 37°C. Cell suspensions were centrifuged and resuspended in Dulbecco's Modified Eagle Medium (DMEM; Gibco)

containing 10% fetal bovine serum (FBS; Gibco) and 1% antibiotics. Primary cells (P0) were expanded until reaching 80–90% confluence and subsequently passaged. Cells at passages 3–4 were used for experiments.

For gingival epithelial cells (GECs), tissues were subjected to cold enzymatic digestion with 0.4% collagenase IV for 24 h at 4°C. Epithelial sheets were mechanically separated and further digested with 0.25% trypsin–EDTA for 15 min. Cells were cultured in defined keratinocyte-serum-free medium (Gibco).

### 2.2. Bioprinting of scaffolds

The bioink formulations employed were: (i) 5 wt% GelMA; (ii) 5 wt% GelMA + 1 wt% ChsMA; and (iii) 5 wt% GelMA + 3 wt% ChsMA. GelMA and ChsMA were purchased from Engineering For Life Bioscience, China.

For the cell-laden constructs (AGH), passage 3–4 GFs were harvested with 0.25% trypsin–EDTA, centrifuged, and resuspended in the prewarmed bioink at a final density of $2 \times 10^6$ cells/mL. The acellular hydrogel (GC) used the same polymer formulations without cells. All printing procedures were performed using a pneumatic extrusion bioprinter equipped with a 25G stainless-steel nozzle. The printing pressure and speed were kept constant for all groups (pressure: 15–20 kPa; speed: 5 mm/s) to ensure dimensional consistency.

Immediately after printing, the constructs were crosslinked under 405 nm visible light (10 mW/cm$^2$) for 60 s to obtain stable hydrogels. For *in vitro* experiments, hydrogels were printed and cultured in complete DMEM. For *in vivo* implantation, GC and AGH constructs were printed using the same protocol and then trimmed into slabs of identical length, width, and thickness to fit the buccal gingival flap area.

In this study, GC used in cell and animal experiments refers to 5 wt% GelMA + 3 wt% ChsMA, and AGH refers to cell-laden GC.

### 2.3. Physicochemical characterization

For morphological analysis, lyophilized scaffolds were gold-sputtered (10 nm) and imaged using scanning electron microscopy (SEM; Zeiss SIGMA HD, Germany; 5 kV).

Rheological properties were evaluated through dynamic oscillatory measurements performed on a rotational rheometer (AR-G2, TA Instruments, USA) with a 20 mm cone–plate geometry. Measurements were conducted at 37°C under 1% strain and 1 Hz frequency, and the storage modulus (*G*') and loss modulus (*G*") were recorded over a 10-min period.

Mechanical testing was performed using a universal testing machine (Instron 5567, USA) equipped with a 0.1 N load cell, and the compressive modulus was determined at a strain rate of 1 mm/min.

### 2.4. Water contact angle measurement

Contact angles were measured at room temperature using a contact angle goniometer (OCA 20, DataPhysics Instruments, Germany). A 2–3 μL droplet of deionized water was gently deposited onto the hydrogel surface using a microsyringe, and images were captured within 5 s of droplet placement. The left and right contact angles were automatically calculated by the instrument software, and their mean value was recorded as the contact angle for each droplet.

### 2.5. Biocompatibility assessment

Biocompatibility was assessed using the Cell Counting Kit-8 (CCK-8) assay, viability staining, and cytoskeletal analysis: Sterile hydrogel discs of each formulation (5% GelMA, 5% GelMA + 1% ChsMA, and 5% GelMA + 3% ChsMA) were prepared as described above, and cells cultured on tissue culture plates without hydrogels served as the control group. Relative cell numbers were quantified by measuring optical density at 450 nm using a microplate reader (Multiskan FC, Thermo Fisher Scientific, USA).

Cell viability was further examined using acridine orange/ethidium bromide dual staining (Beyotime Biotechnology, China) on days 1, 3, 5, and 7, and live/dead cell ratios were analyzed by fluorescence microscopy (Zeiss Axio Observer).

For cytoskeletal organization, AGH constructs were fixed with 4% paraformaldehyde for 30 min and permeabilized with 0.5% Triton X-100 for 10 min. F-actin was stained with rhodamine phalloidin (1:200; Cytoskeleton, USA), and nuclei were labeled with 4',6-diamidino-2-phenylindole (DAPI; 1:1000; Thermo Fisher, USA). 3D morphology was reconstructed using confocal laser scanning microscopy (Zeiss LSM 880).

### 2.6. Scratch wound assay

Confluent monolayers of GFs and GECs in six-well plates were scratched with a sterile 200 μL pipette tip. Detached cells were removed by washing with PBS, and the cultures were then maintained in low-serum medium (2% FBS). Cell migration was monitored over a 24-h period. Experimental groups included GFs (tissue-culture-plastic–grown fibroblasts), GC (hydrogel-only material control), and AGH.

### 2.7. Single-cell RNA sequencing data analysis

Publicly available single-cell RNA-sequencing data were obtained from the Gene Expression Omnibus dataset

GSE164241, which contains transcriptional profiles of human gingival mucosa and oral buccal mucosa. Raw data were processed using Seurat v4.1.1 (Satija Lab USA). Quality control included removal of genes expressed in fewer than three cells and exclusion of cells with >20% mitochondrial gene content. Data were normalized by SCTransform with 3,000 variable features. Clustering was performed using Uniform Manifold Approximation and Projection (resolution = 0.6), and differentially expressed genes were identified using the FindMarkers function.

### 2.8. Quantitative reverse transcription polymerase chain reaction analysis

Complementary DNA (cDNA) was synthesized from total RNA using a reverse transcription kit (Takara, Japan) and subsequently amplified with SYBR Green Master Mix (Roche, Switzerland). Relative gene expression was calculated using the 2^−ΔΔCt method. The primer sequences used for each target gene are listed in Table 1.

### 2.9. Western blotting

Proteins were extracted, separated by sodium dodecyl sulfate–polyacrylamide gel electrophoresis, and transferred onto polyvinylidene fluoride membranes. After blocking with 5% BSA, membranes were incubated with primary antibodies (β-catenin, N-cadherin, COL-I, SMAD2/3/4) overnight at 4°C, followed by incubation with horseradish peroxidase-conjugated secondary antibodies. Chemiluminescent signals were detected using ECL Prime (GE Healthcare, USA) and quantified with Image-Pro Plus 6.0 (Media Cybernetics, USA).

### 2.10. Immunofluorescence

Cells or tissue sections were incubated with primary antibodies overnight at 4°C, followed by rhodamine-conjugated anti-rabbit IgG (1:200; Invitrogen, USA). Nuclei were counterstained with DAPI (5 μg/mL). Images were acquired using a Zeiss Axio Imager M2 microscope.

### 2.11. Animal models and groupings

Eight-week-old Sprague–Dawley rats ($n$ = 3) were used. A partial-thickness flap was raised on the buccal side of the maxillary incisors by a mesiodistal incision. The control group received direct suturing, whereas the experimental groups received implantation of GC or AGH under the flap before suturing. Animals were randomly assigned to the control, GC, or AGH groups. This study was carried out following the recommendations of the Animal Care and Experiment Committee of Shanghai Ninth People's Hospital, Shanghai Jiao Tong University School of Medicine. The protocol was approved by the Animal Care and Experiment Committee of Shanghai Ninth People's Hospital, Shanghai Jiao Tong University School of Medicine (SH9H-2024-A1046-SB), and conducted in accordance with institutional guidelines for the care and use of laboratory animals and the Animal Research: Reporting of *In Vivo* Experiments recommendations.

### 2.12. Magnetic resonance imaging

At 6 weeks after surgery, gingival thickness was evaluated using a small-animal magnetic resonance imaging (MRI) system (Bruker BioSpin MRI GmbH, Germany). Rats were anesthetized and placed in a prone position in a dedicated animal cradle, with the maxillary incisors aligned along a predefined reference line to standardize head orientation. T2-weighted coronal images of the maxillary incisor region were acquired using a rapid acquisition with relaxation enhancement sequence.

To minimize spatial variability, coronal slices were obtained perpendicular to the long axis of the maxillary incisors. Gingival thickness was measured at the mid-buccal aspect of the incisors using the cemento–enamel junction and incisal edge as anatomical landmarks. For each animal, measurements were taken on three consecutive slices centered on the mid-buccal site; the distances from the outer gingival surface to the underlying hard-tissue reference plane were recorded and averaged to obtain a single gingival thickness value per site. Image analysis was performed in ImageJ (Developer, Country) by a single examiner blinded to group allocation. Repeated measurements on a randomly selected subset of scans confirmed good intra-observer reproducibility.

After MRI acquisition, animals were euthanized, and the maxillary anterior segments were harvested for subsequent histological and immunohistochemical analyses.

**Table 1. Primer sequences used for quantitative reverse transcription polymerase chain reaction**

| Gene name | Forward | Reverse |
|---|---|---|
| Col1a1 | 5'-CCTGGTAAAGATGGTGCC-3' | 5'-CACCAGGTTCACCTTTCG-3' |
| Fn | 5'-GACCTGACAGTCGGAGAAG-3' | 5'-TGACACGGAGTAACGGTTC-3' |
| Krt10 | 5'-GAGGAGCTGCTGAAGAAGG-3' | 5'-CTGGTGGTGTTGTTGATGG-3' |
| Krt14 | 5'-CCAGACCTACAGCAACAGC-3' | 5'-GGTCCAGGTTCTCTTGGTG-3' |
| Gapdh | 5'-GATGCCTGCTTCACCACCT-3' | 5'-GTGGTGCAGGATGCATTGCT-3' |

### 2.13. Histological staining

Samples were fixed in formalin, dehydrated through a graded ethanol series, and embedded in paraffin. Sections (5 μm) were stained with hematoxylin and eosin (H&E) and Masson's trichrome and examined under an optical microscope.

For immunohistochemistry, sections were rehydrated, subjected to antigen retrieval, and incubated overnight at 4°C with a cluster of differentiation (CD)34 antibody (1:100; Abcam, Country). A biotinylated secondary antibody and avidin–biotin–peroxidase complex were applied, and staining was visualized with 3,3'-diaminobenzidine substrate. Sections were counterstained with hematoxylin, mounted, and examined microscopically.

### 2.14. Statistical analysis

All data are presented as mean ± standard deviation. Comparisons between two groups were performed using independent-samples *t*-tests. One-way analysis of variance was used for multiple group comparisons in GraphPad Prism 9.0 (Developer, Country). A $p$-value < 0.05 was considered statistically significant.

## 3. Results

### 3.1. Physicochemical properties of 3D-bioprinted scaffolds

Figure 1A shows that rheological experiments confirmed the normal photocuring behavior of GelMA and GelMA–ChsMA hydrogels. Prior to 405 nm light irradiation, all groups exhibited a *G*" higher than the *G*', indicating that the inks remained in a liquid state and underwent viscous deformation. After 30 s of irradiation, *G*' exceeded *G*", confirming the transition into a hydrogel. Among all formulations, the 5% GelMA + 3% ChsMA displayed a significantly higher *G*' (approximately 3.7 kPa) compared with the other groups (Figure 1B).

As shown in Figure 1C, the stress–strain curves of all three groups exhibited nonlinear elastic behavior within the 40% strain range. Furthermore, Figure 1D demonstrates that the compressive strength of the 5% GelMA + 3% ChsMA group reached 6.4 kPa, which was significantly greater than that of the other formulations.

Figure 1E illustrates that the printed constructs in all groups maintained intact, interconnected grid structures without evidence of pore collapse. SEM images corroborated the presence of open, porous architectures with uniformly distributed macropores. As the ChsMA concentration increased, well-aligned microfilaments with distinct boundaries were observed (Figure 1F). The 5% GelMA + 3% ChsMA group exhibited smaller and more uniformly distributed pores compared with the 5% GelMA + 1% ChsMA group.

Surface wettability of the hydrogels was evaluated by static water contact angle measurements (Figure 1). Pure 5% GelMA exhibited a moderate contact angle of

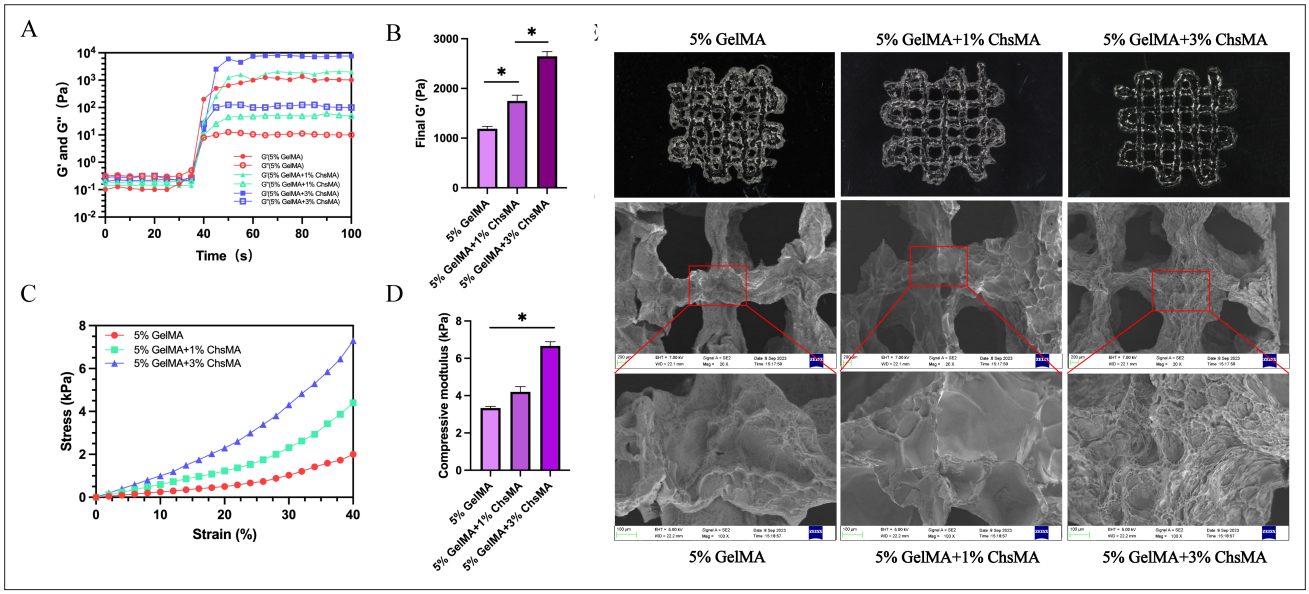


**Figure 1.** Rheological and physicochemical properties and morphology of 3D-bioprinted scaffolds. (A) Light-curing process of scaffolds with different groups. (B) Final storage modulus (*G*') after curing. (C) Stress–strain curves of different groups. (D) Compressive modulus of different groups. (E) Morphology of printed constructs captured using digital camera. (F) Scanning electron microscopy images of different groups (magnifications = 20× [top panels], 100× [bottom panels]; scales = 200 μm [top panels], 100 μm [bottom panels]). Notes: *$p$ < 0.05, **$p$ < 0.01, ***$p$ < 0.001; $n$ = 3. Abbreviations: ChsMA, Chondroitin sulfate methacrylate; GelMA, Gelatin methacrylate.

approximately 77.5°, whereas the incorporation of ChsMA markedly increased surface hydrophilicity, decreasing the contact angle to about 57.5° for 5% GelMA + 1% ChsMA and 46.0° for 5% GelMA + 3% ChsMA. Thus, higher ChsMA content resulted in a progressively more hydrophilic hydrogel surface.

The effects of different hydrogel compositions on GF viability and proliferation were further evaluated by CCK-8 assay over 7 days (Figure S2). In all groups, including the plate-cultured control as well as the 5% GelMA, 5% GelMA + 1% ChsMA, and 5% GelMA + 3% ChsMA hydrogels, OD450 values increased continuously from day 1 to day 7, indicating sustained cell growth without detectable cytotoxicity. At each time point, no statistically significant differences in cell proliferation were observed among the hydrogel formulations or between the hydrogel groups and the control.

Collectively, these characterization results demonstrate that the 5% GelMA + 3% ChsMA bioink possesses favorable rheological and mechanical properties suitable for extrusion-based bioprinting. Therefore, 5% GelMA + 3% ChsMA was selected as the working composition for all subsequent cell culture and *in vivo* experiments.

### 3.2. Identification of gingiva-specific extracellular matrix-remodeling signatures by single-cell transcriptomic profiling

To investigate the intrinsic molecular characteristics of GFs, we reanalyzed the public single-cell RNA-sequencing dataset GSE164241, which includes gingival and oral mucosal tissues. Unsupervised clustering revealed four major cell compartments—epithelial (*KRT14*, *KRT5*, *S100A2*, *CTSA*, *SPRR1B*), fibroblast (*LUM*, *COL3A1*, *DCN*, *COL1A1*, *CFD*), endothelial (*ACKR1*, *RAMP2*, *SELE*, *VWF*, *PECAM1*), and immune populations (*CD69*, *CD52*, *CXCR4*, *PTPRC*, *HCST*)—each expressing canonical markers (Figure 2A and B).

Comparison of tissue composition showed similar proportions of major cell types between the gingiva and oral mucosa (Figure 2C). Reclustering of fibroblasts further identified four transcriptionally distinct subpopulations

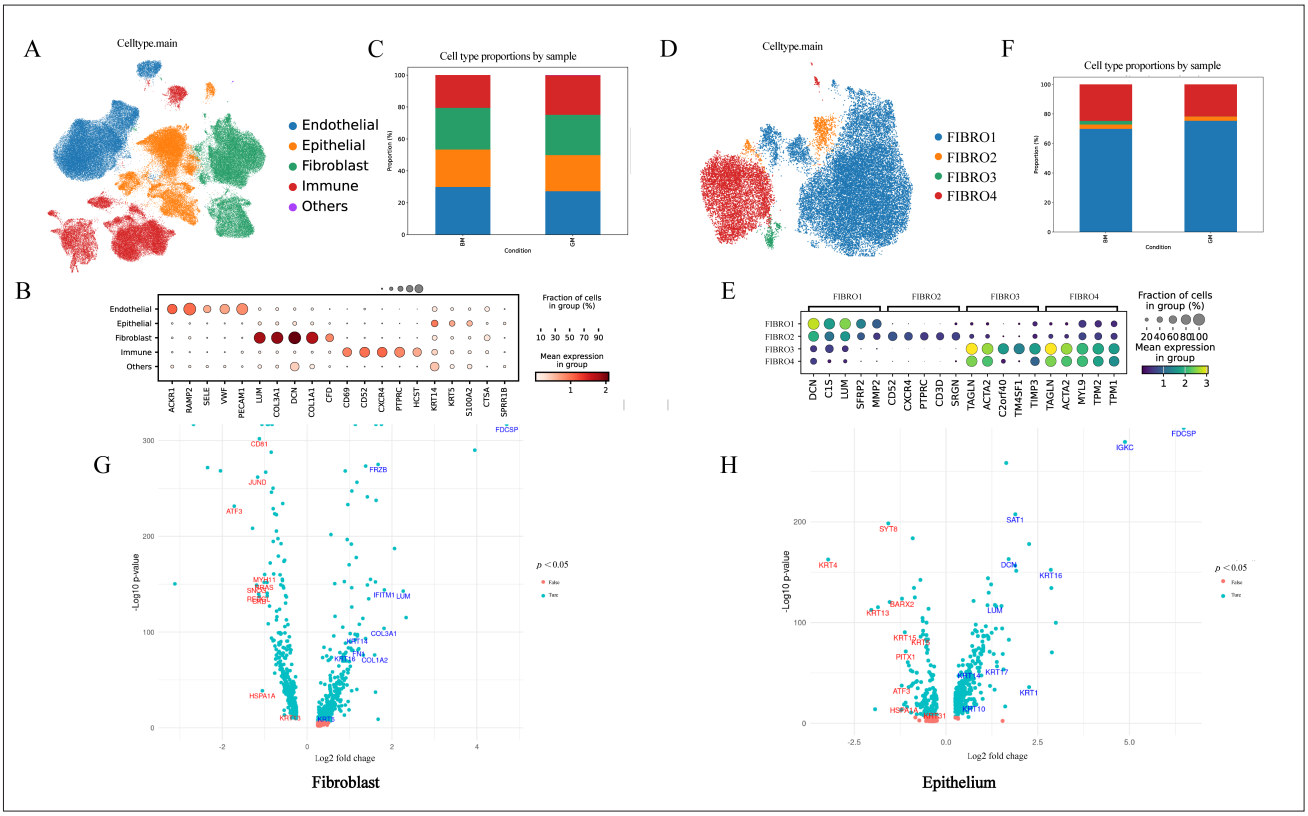


**Figure 2.** Differential gene expression between fibroblasts and epithelial cells in oral mucosa and gingiva. (A) After dimensionality reduction and clustering, five cell subpopulations were identified. (B) Bubble plots displaying signature gene expression in each cell type. (C) Proportion of different cell subpopulations in the gingiva and oral mucosa. (D) Reclustering of fibroblasts identified four subtypes. (E) Bubble plots showing signature gene expression in each fibroblast subtype. (F) Proportion of fibroblast subpopulations in the gingiva and oral mucosa. (G) Volcano plot exhibiting differential gene expression in gingival and oral mucosal tissue fibroblasts. (H) Volcano plots displaying differential gene expression in gingival and oral mucosal tissue epithelial cells. Note: Red, downregulated genes; blue, upregulated genes.

(Figure 2D). Among these, FIBRO1 displayed a matrix-remodeling phenotype characterized by high expression of *DCN*, *LUM*, *COL3A1*, and other ECM-associated genes (Figure 2E). This population was enriched in gingival tissue (Figure 2F), suggesting the presence of a gingiva-specific fibroblast subset with enhanced regenerative potential.

Differential gene expression analysis further demonstrated that GFs exhibited significantly elevated expression of key ECM components, including *COL1A1* and *FN1*, compared with oral mucosal fibroblasts (Figure 2G and H). These two genes are central regulators of collagen organization, cell adhesion, and tissue remodeling. In contrast, epithelial cells showed higher levels of keratinization-related genes *KRT10* and *KRT14*.

Collectively, the single-cell analysis highlights that GFs possess a distinct ECM-remodeling signature dominated by *COL1* and *FN*, providing a strong biological rationale for selecting these genes as downstream molecular readouts in our hydrogel-based experiments.

### 3.3. Biocompatibility of active gingival hydrogel and upregulation of extracellular matrix-related genes in gingival fibroblasts

Live/dead staining showed that GFs maintained high viability within the hydrogel throughout the 1-, 3-, 5-, and 7-day culture period, with only a few nonviable cells appearing at later time points (Figure 3A). These findings indicate that the GelMA/ChsMA matrix provides a permissive environment for cell survival. Cytoskeleton staining further revealed progressive morphological changes: fibroblasts initially appeared rounded but

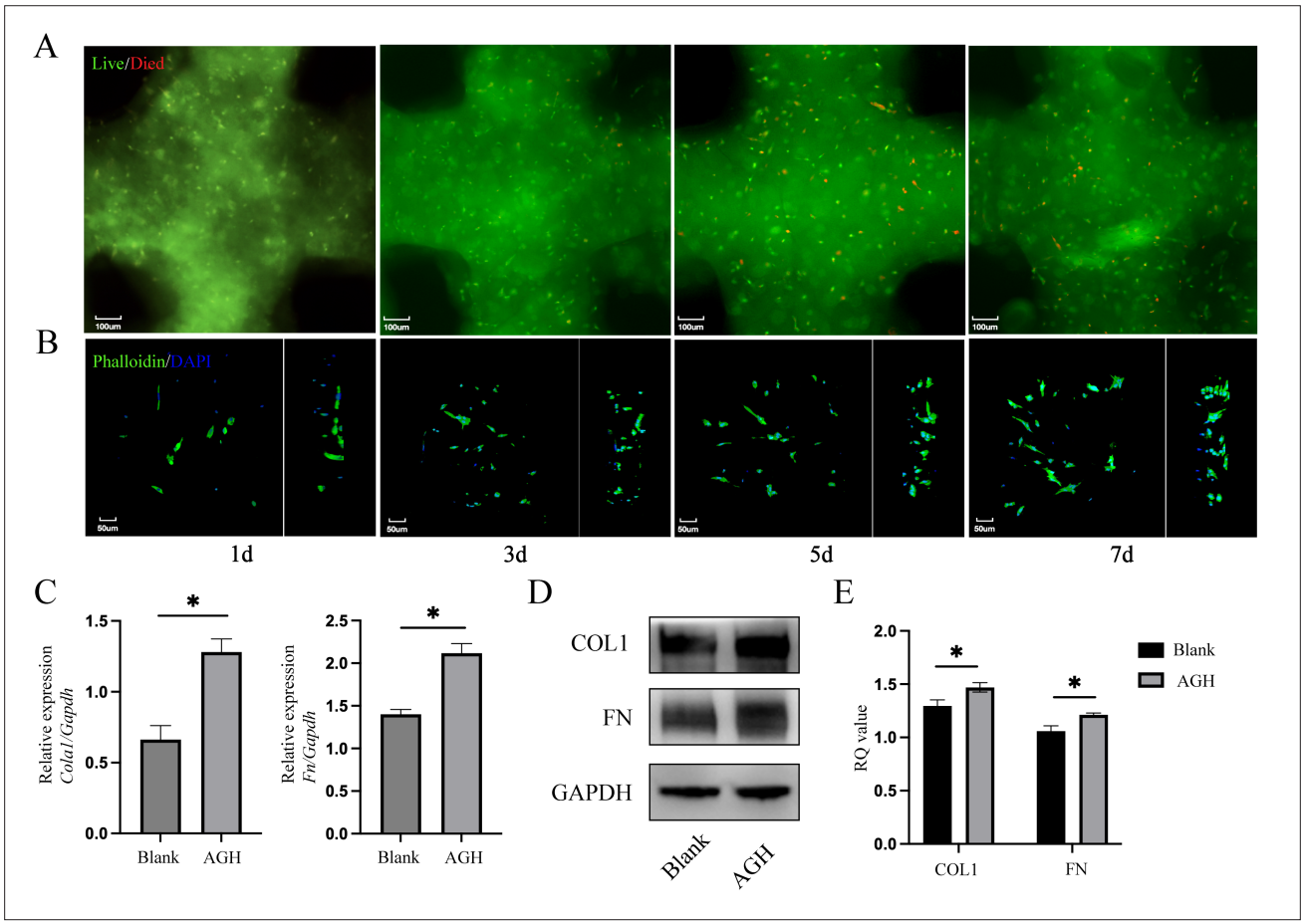


**Figure 3.** Biocompatibility and promotion of extracellular matrix synthesis by the bioink. (A) Live-dead staining of gingival fibroblasts in bioprinted scaffolds (magnification = 200×; scale = 100 μm). (B) Cytoskeletal staining of gingival fibroblasts in bioprinted scaffolds (magnification = 400×; scale = 50 μm). (C) Relative gene expression of *Col1a1* and *Fn* in bioprinted gingival fibroblast scaffolds. (D) Protein expression levels of COL1 and FN in bioprinted gingival fibroblast scaffolds. (E) Quantification of COL1 and FN expression. Notes: Blank: Tissue culture control. $^{*}p < 0.05$, $^{**}p < 0.01$, $^{***}p < 0.001$; $n = 3$. Abbreviations: AGH, Active gingival hydrogel; COL1, Collagen type 1; d, Day(s); FN, Fibronectin; GAPDH, Glyceraldehyde 3-phosphate dehydrogenase.

gradually expanded along the hydrogel network, displaying polygonal cell bodies and distinct pseudopodia by day 7 (Figure 3B). Such cytoskeletal organization is consistent with enhanced adhesion and early migratory activity within the 3D microenvironment.

At the molecular level, cells cultured in AGH showed significantly elevated transcription of *Col1a1* and *Fn* compared with cells cultured on standard tissue culture plastic (Figure 3C). Western blot analysis confirmed the corresponding increase in protein levels (Figure 3D), and quantification of band intensities further supported this trend (Figure 3E). Immunofluorescence staining also demonstrated more abundant and organized deposition of COL1 and FN within the AGH constructs, reflecting active matrix remodeling by the embedded fibroblasts.

Together, these observations show that the AGH not only supports fibroblast survival but also promotes their adhesion, spreading, and ECM production. The coordinated upregulation of COL1 and FN—two key structural proteins essential for matrix remodeling and cell–matrix interactions—indicates that GFs actively engage with and remodel the printed hydrogel, providing a biological foundation for subsequent tissue regeneration.

### 3.4. Effects of active gingival hydrogel on fibroblast activity and epithelial keratinization

Gingival fibroblasts were cultured under three conditions: tissue culture plastic (GFs), acellular hydrogel (GC), and AGH, respectively. Cytoskeletal staining (Figure 4A) revealed that fibroblasts in the AGH group exhibited superior spreading morphology compared with those in the GFs and GC groups. Specifically, AGH-treated cells displayed a pronounced polygonal shape, broader spreading, more uniform cytoskeletal distribution, thicker actin fibers, and enhanced structural integrity.

Scratch assay results (Figure 4B) showed that the AGH group achieved the fastest wound closure, with the smallest residual scratch area at 24 hours. Consistently, Western blotting (Figure 4C and D) and immunofluorescence staining (Figure 4E and F) demonstrated that *Col1a1* and *Fn* expression in fibroblasts was significantly elevated in the AGH group. Furthermore, when AGH was cocultured with GECs, transcription levels of *Krt10* and *Krt14* were upregulated (Figure 4G and H), suggesting a potential role for AGH in promoting epithelial differentiation and keratinization.

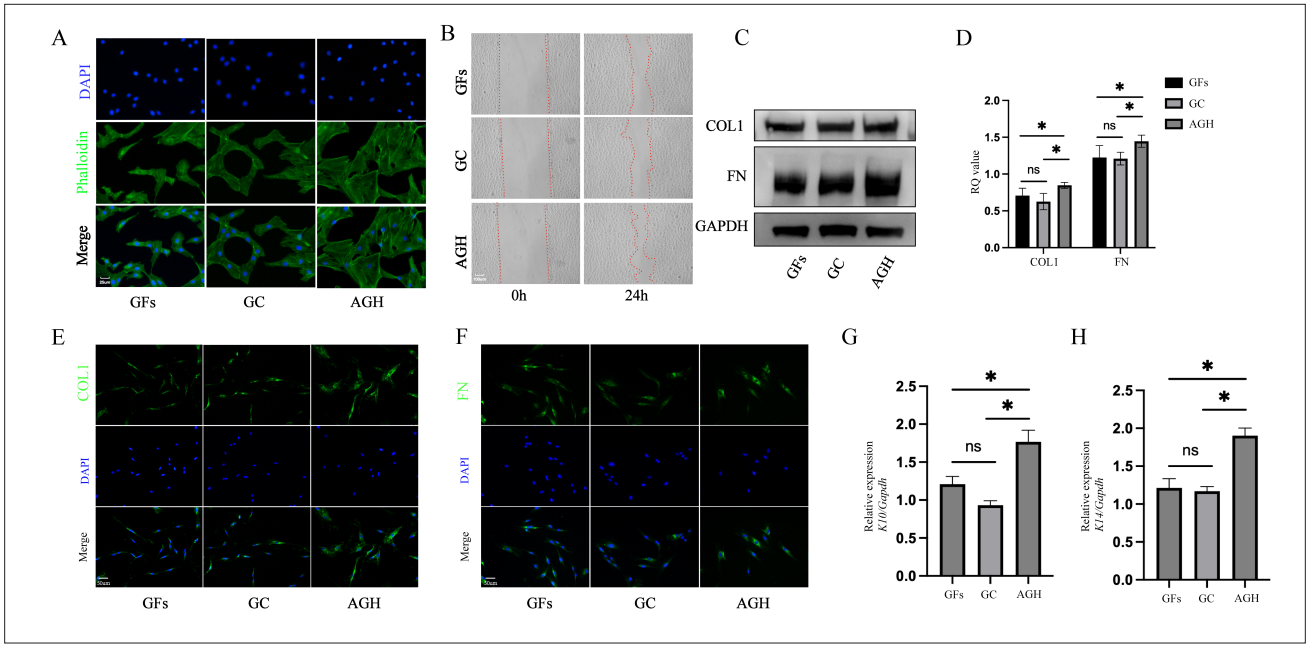


**Figure 4.** The impact of bioprinted scaffolds on gingival fibroblasts and epithelial cells. (A) Gingival fibroblast adhesion (magnification = 800×; scale = 25 μm). (B) Gingival fibroblast migration (magnification = 200×; scale = 100 μm). (C) Protein expression of COL1 and FN in gingival fibroblasts. (D) Quantification of COL1 and FN proteins in WB. (E,F) Immunofluorescence staining of COL1 and FN in gingival fibroblasts treated with GFs, GC, and AGH for 24 h (magnifications = 400× [E], 400× [F]; scales = 50 μm [E], 50 μm [F]). (G,H) Relative gene expression of K10 and K14 in epithelial cells. Note: $^{*}p < 0.05$, $^{**}p < 0.01$, $^{***}p < 0.001$; $n = 3$. Abbreviations: AGH, Active gingival hydrogel; COL, Collagen type 1; DAPI, 4',6-diamidino-2-phenylindole; FN, Fibronectin; GAPDH, Glyceraldehyde 3-phosphate dehydrogenase; GC, Acellular hydrogel; GFs, Gingival fibroblasts; ns, Not significant.

### 3.5. Activation of Wnt/β-catenin and transforming growth factor-β/Smad signaling pathways by active gingival hydrogel

COL1 and FN are well-recognized ECM components that can activate Wnt/β-catenin and TGF-β/Smad signaling pathways, both of which play critical roles in fibroblast-mediated tissue remodeling and keratinization. These findings suggest that the FIBRO1 subpopulation may contribute to postgrafting keratinization in nonkeratinized epithelium through ECM–signaling interactions.

To further investigate the underlying mechanisms, we examined the involvement of the Wnt/β-catenin and TGF-β/Smad pathways. Western blotting and immunofluorescence revealed that AGH markedly upregulated the expression of β-catenin and N-cadherin compared with the other groups, and this effect was reversed by the Wnt/β-catenin pathway inhibitor methyl-sulfonyl AB (Figure 5A–C). In parallel, analysis of SMAD signaling showed that the levels of phosphorylated SMAD2, SMAD3, and SMAD4 were significantly increased in the AGH group (Figure 5D–G).

### 3.6. *In vivo* gingival thickening, collagen deposition, and angiogenesis with active gingival hydrogel

As shown in Figure 6A, GC and AGH constructs were implanted beneath partial-thickness flaps of rat incisor gingiva. Six weeks after implantation, T2-weighted small animal MRI scans enabled a clear distinction between hard tissue (dark signal) and soft tissue (bright signal). Quantitative measurements at multiple sites demonstrated that gingival thickness in the AGH group was significantly greater than that in the GC and blank groups (Figure 6B and F). Importantly, MRI provided a noninvasive and dynamic approach to monitor gingival soft tissue augmentation, highlighting its value as a translational tool.

Histological evaluation further supported these findings. H&E and Masson's trichrome staining (Figure 6C and D) showed well-preserved tissue boundaries and

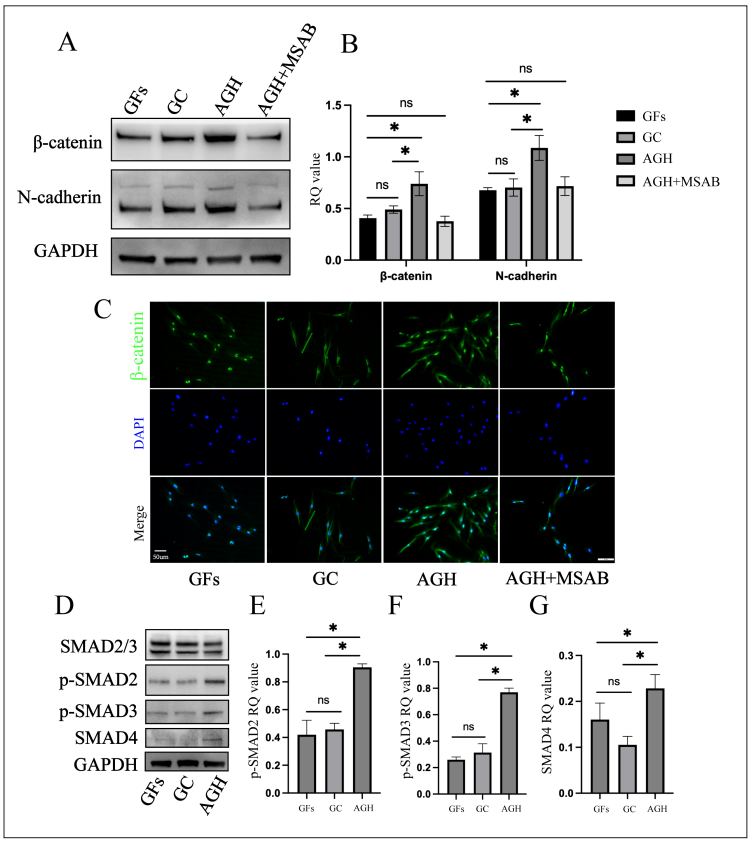


**Figure 5.** Activation of Wnt/β-catenin and SMAD signaling in gingival fibroblasts. (A) Western blot analysis of β-catenin and N-cadherin in gingival fibroblasts. (B) Quantification of β-catenin and N-cadherin expression. (C) Immunofluorescence of β-catenin (green) in gingival fibroblasts (magnification = 400×; scale = 50 μm). (D) Western blot analysis of SMAD pathway proteins: SMAD2/3, p-SMAD2, p-SMAD3, and SMAD4. (E–G) Quantification of SMAD pathway proteins. Notes: $^{*}p < 0.05$, $^{**}p < 0.01$, $^{***}p < 0.001$; $n = 3$. Abbreviations: AGH, Active gingival hydrogel; DAPI, 4',6-diamidino-2-phenylindole; GAPDH, Glyceraldehyde 3-phosphate dehydrogenase; GC, Acellular hydrogel; GFs, gingival fibroblasts; MSAB, Methyl-sulfonyl AB; ns, Not significant.

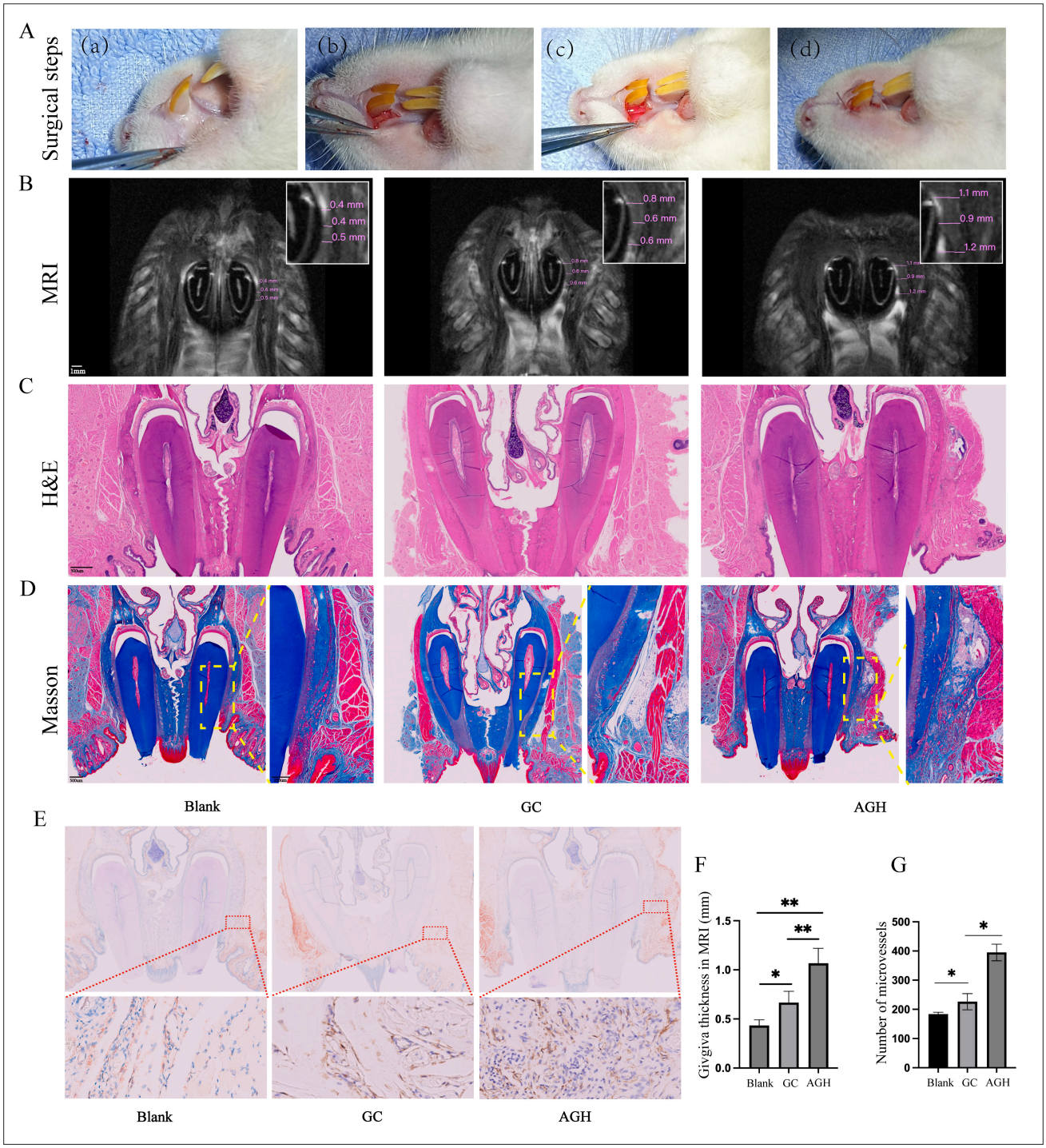


**Figure 6.** *In vivo* gingival augmentation using bioprinted scaffolds. (A) Surgical procedure: (a) preoperative view, (b) elevation of partial-thickness flap, (c) scaffold implantation, (d) suturing. (B) T2-weighted magnetic resonance imaging (MRI) images of the gingiva. (C) Hematoxylin and eosin (H&E)-stained gingival sections (magnifications = 4×; scales = 500 μm). (D) Masson's trichrome-stained sections (magnifications = 4×, 8×; scales =500 μm ,250 μm). (E) Immunohistochemical staining of CD34 (magnifications = 4×, 40×; scales =500 μm ,50 μm). (F) Quantification of gingival thickness from MRI. (G) Quantification of microvessel density in immunohistochemistry. Notes: Blank, Sham operation; GC, Hydrogel-only control. $^{*}p < 0.05$, $^{**}p < 0.01$, $^{***}p < 0.001$; $n = 3$. Abbreviations: AGH, Active gingival hydrogel; CD34, Cluster of differentiation 34.

intact layer structures without tearing or damage. The gingival epithelium consisted of multiple cell layers, while the lamina propria contained abundant vasculature and crisscrossed collagen fibers supporting epithelial attachment. After 6 weeks, the hydrogel was fully degraded. In the AGH group, newly formed connective tissue was evident, accompanied by mild infiltration of inflammatory cells. Masson's staining revealed substantial new collagen deposition, consistent with enhanced ECM remodeling.

Immunohistochemical staining of CD34 confirmed a markedly higher density of neovascularization in the AGH group compared with the other groups (Figure 6E and G). Collectively, these results indicate that AGH promotes gingival thickening, collagen deposition, and angiogenesis, while MRI provides a novel, noninvasive strategy for evaluating periodontal soft tissue regeneration *in vivo*.

## 4. Discussion

We prepared a new photocrosslinkable polymer ink composed of ChsMA and GelMA. The combination of GelMA and ChsMA addresses the three major challenges faced by traditional biomaterials in gingival augmentation—insufficient structural precision, lack of bioactivity, and poor mechanical adaptability—through biomimetic ECM components, tunable mechanical properties, and multifunctional synergistic effects.

Single-cell transcriptomic analysis was incorporated into this study to clarify the intrinsic biological features of GFs that are directly relevant to soft-tissue regeneration. Reanalysis of the GSE164241 dataset revealed that GFs—compared with oral mucosal fibroblasts—displayed markedly higher expression of ECM-associated genes, such as *COL1A1* and *FN1*, as well as members of the small leucine-rich proteoglycan family (e.g., *LUM*, *DCN*), which are known regulators of collagen fibrillogenesis and matrix organization. These findings are consistent with prior oral wound-healing studies showing that gingival connective tissue possesses a unique molecular profile characterized by faster matrix turnover, reduced fibrosis, and more efficient remodeling.[16] Importantly, the transcriptomic analyses of GFs and epithelial cells were not conceived as a separate exploratory block but rather as the biological foundation for our bioink design. The enrichment of Fn and COL1 in GFs, together with higher KRT10 and KRT14 expression in gingival epithelium compared with oral mucosa, highlighted gingiva-derived fibroblasts as a cell source intrinsically geared toward ECM remodeling and keratinization. These observations directly informed our decision to use GFs in the GelMA/ChsMA bioink and to focus on FN/COL1 and KRT10/KRT14 as functional readouts of the 3D-bioprinted constructs. The subsequent *in vitro* and *in vivo* results—showing FN/COL1 upregulation, activation of Wnt/β-catenin and TGF-β/Smad signaling, and increased KRT10/KRT14 expression—therefore represent a mechanistic realization of the transcriptomic profile identified at the beginning of the study.

Rheological characteristics of hydrogels and bioinks play a crucial role in extrusion-based bioprinting.[22] Successful printing relies on the formation of a stable flow filament during extrusion and sufficient mechanical strength to maintain the structural integrity of the printed constructs afterward.[23] The compressive strength of GC reached 6.4 kPa, a level that not only imparts adequate mechanical strength to the hydrogel but also matches the biomechanical properties of natural gingiva.[24] Its relatively soft texture and high water content enable GFs to continue growing, proliferating, and secreting/depositing collagen fibers after printing. The gradual decrease in contact angle with increasing ChsMA content indicates that GelMA/ChsMA hydrogels become progressively more hydrophilic. This trend is consistent with the highly polar, anionic nature of chondroitin sulfate, which introduces additional carboxyl and sulfate groups into the network and enhances water–polymer interactions.

Gelatin methacrylate, with its RGD motifs and tunable stiffness, replicates the gingival lamina propria's biomechanics while supporting fibroblast adhesion.[25] ChsMA complements this by emulating glycosaminoglycan-rich ECMs and enhancing COL1/COL3 synthesis. This material strategy not only offers a promising new solution for soft-tissue regeneration but also lays the foundation for personalized medicine and precision dental treatment.[26-28] The GC hydrogel possesses an appropriate pore size and porosity, which enable cells to stretch and migrate freely. This suitable pore structure provides sufficient space for cells and facilitates nutrient and waste exchange, maintaining normal physiological function and promoting cell adhesion and migration.

Animal experiments and clinical studies have shown that the connective tissue beneath the epithelium of keratinized gingiva can induce surface epithelial cells to differentiate into keratinized gingival epithelium.[14,15] Fibroblasts, as the main cellular component of the connective tissue, play a significant role in this transformation process. They primarily originate from mesenchyme, and their main function is to synthesize ECM, providing a physical scaffold for cellular activity and promoting rapid tissue repair following tissue injury.[29] Anatomically, fibroblasts can be categorized into reticular-layer and papillary-layer fibroblasts.[30] However, fibroblasts may also exhibit functional diversity within the same anatomical location,

indicating that simple anatomical stratification is no longer sufficient to understand fibroblast heterogeneity.

Fibroblasts proliferate within the hydrogel and form a unique microenvironment that promotes FN secretion by GFs. FN binds to integrin receptors on the cell surface and activates intracellular signaling pathways, such as the focal adhesion kinase/Src kinase pathway, thereby regulating focal adhesion formation and actin cytoskeleton reorganization, which together facilitate cell migration. COL1 increases adhesion between cells and the hydrogel, and its fibrous structure also provides directional cues for cell migration.[31]

In the classic Wnt/β-catenin signaling pathway, binding of the Wnt ligands to the Frizzled receptor and the low-density lipoprotein receptor-related protein 5/6 coreceptor inhibits glycogen synthase kinase-3β activity, preventing β-catenin degradation. Accumulated β-catenin in the cytoplasm translocates to the nucleus, binds to the T-cell factor (TCF)/lymphoid enhancer factor transcription factors, and regulates downstream gene expression.[32] FN has been identified as a target gene regulated by β-catenin/TCF transcription. TGF-β, an important cytokine, activates receptor-regulated SMADS, such as SMAD2 and SMAD3. These activated SMADS form heteromultimers with SMAD4 and are transported into the nucleus to regulate the expression of various target genes, including *COL1* and *FN*. In many cell types, such as fibroblasts, TGF-β stimulation significantly upregulates *COL1* and *FN* expression via the SMAD pathway, promoting ECM synthesis and deposition. The SMAD pathway can also interact with other signaling cascades, such as phosphoinositide 3-kinase/protein kinase B and mitogen-activated protein kinase, to jointly regulate *COL1* and *FN* expression.[33]

Current approaches to assessing gingival thickness include direct and imaging-based methods, each with specific advantages and limitations. Direct techniques include probe estimation, which is simple but subjective, and surgical flap measurement, which is accurate but invasive and carries a risk of tissue damage.[34,35] Imaging modalities offer noninvasive alternatives: cone-beam computed tomography provides 3D visualization but suffers from limited soft-tissue resolution and radiation exposure, while ultrasound is operator-dependent and less reliable in thick tissues. MRI has emerged as an optimal preclinical tool due to its superior soft-tissue contrast (<0.5 mm resolution), absence of radiation, and ability to visualize multilayered gingival structures—features that are critical for longitudinal studies in rodent models.[36,37] In our current study, MRI was used for the first time to evaluate gingival thickness in living rats. Its high soft-tissue resolution enabled direct visualization of gingival thickness changes following AGH implantation. Another important consideration is the degradation behavior of the GC/AGH hydrogels. In the present study, we did not perform a dedicated quantitative analysis of *in vivo* mass loss. Instead, gingival thickness was assessed using MRI as the distance between the soft-tissue surface and the underlying hard-tissue reference plane. At the 6-week endpoint, histological sections did not reveal clearly demarcated remnants of dense, acellular hydrogel; instead, the implantation sites were replaced by vascularized connective tissue rich in collagen fibers, suggesting substantial substitution of the initial matrix by host tissue. Nevertheless, we cannot completely rule out the presence of small residual hydrogel fragments that may still contribute to the soft-tissue volume signal on MRI. Future studies will therefore incorporate labeled or otherwise trackable hydrogels, along with earlier and extended observation time points, to more precisely correlate *in vivo* degradation kinetics with dynamic changes in gingival thickness and collagen remodeling.

3D bioprinting emerges as a transformative strategy by enabling the precise fabrication of vascularized, anatomically tailored constructs.[38] Unlike conventional substitutes, this technology allows layer-specific deposition of cells and biomaterials, thereby reconstructing the epithelial–stromal interface and microvascular networks that are essential for graft integration and long-term stability. Liu *et al.*[39] printed acellular dermal matrix scaffolds encapsulating GFs to increase keratinized gingival width, demonstrating that cell-laden scaffolds promoted soft-tissue regeneration more effectively than cell-free scaffolds, findings that are consistent with our results. However, their research had several limitations, including a small animal sample size, a lack of histological assessments, and the absence of mechanistic analyses. In contrast, our study focused on the equally important phenotype of gingival thickness, not only verifying its efficacy and stability in an animal model but also providing a more in-depth investigation into the mechanisms of regeneration and rekeratinization. These advances highlight the advantages of our material system. Dai *et al.*[40] utilized artificial intelligence to design bioprinted *in vitro* free-gingival substitutes with precise dimensions; however, the lack of animal experiments leaves the *in vivo* regenerative potential of their constructs unresolved.

Although gingival tissue exhibits a remarkable intrinsic healing capacity, this regenerative ability is largely limited to re-epithelialization and defect closure rather than *de novo* thickening of the underlying connective tissue. In the partial-thickness flap model used in this study, untreated sites healed predictably through epithelial coverage, yet connective-tissue volume remained essentially unchanged, as confirmed by MRI and histological results in the control groups. This outcome aligns with clinical observations that

natural healing rarely increases gingival thickness without surgical grafting. In contrast, AGH implantation produced a clear and quantifiable enhancement of soft-tissue volume and collagen deposition, demonstrating a biological effect that exceeds the capacity of spontaneous healing. Therefore, this model well well-suited for evaluating a material's ability to modulate connective-tissue remodeling—a biological outcome not achieved through natural repair alone. This distinction underscores the regenerative advantage of AGH and supports its clinical relevance for soft-tissue augmentation.

In summary, we constructed a bioprintable ink for GFs that forms a hydrogel with good biocompatibility and stable mechanical properties following photocuring. Bioprinting enhances gingival thickness through precise structural replication of the lamina propria, biomimetic bioinks that guide fibroblast proliferation and collagen synthesis, and vascular integration facilitated by embedded angiogenic factors. GFs can proliferate, migrate, and adhere within the construct, and they continue to synthesize ECM components. As a substitute for gingival connective tissue, AGH activates the Wnt/β-catenin and SMAD signaling pathways in GFs and promotes keratinization in GECs. After transplantation *in vivo*, AGH achieved a stable and measurable thickening of the gingiva. Nonetheless, although this study demonstrates clear efficacy in increasing gingival thickness, it lacks sufficient depth regarding the widening of keratinized gingiva and its underlying mechanisms. Future work will therefore focus on material refinement to address these aspects.

## 5. Conclusion

In conclusion, we developed an active gingival hydrogel with favorable mechanical properties and excellent biocompatibility that effectively remodels the gingival phenotype in a rat model. AGH holds substantial promise for periodontal/peri-implant soft-tissue augmentation.

## Acknowledgments

None.

## Funding

This work was supported by the Biomaterials and Regenerative Medicine Institute Cooperative Research Project, Shanghai Jiao Tong University School of Medicine (Project No. 2022LHB04), and the Fundamental Research Program Funding of Ninth People's Hospital Affiliated to Shanghai Jiao Tong University School of Medicine (Project No. JYZZ210). The National Key Research and Development Program of China (2023YFC2413600).

## Conflict of interest

The authors declare that they have no competing interests.

## Author contributions

*Conceptualization:* Zhongchen Song, Guodong Zhou
*Formal analysis:* Han Hu, Yue Liao, Jiachen Dong
*Investigation:* Han Hu, Zhongchen Song
*Methodology:* Han Hu, Xin Sun
*Writing–original draft:* Han Hu
*Writing–review & editing:* Han Hu, Yue Liao, Jiachen Dong, Mengjun Sun, Zhongchen Song

## Ethics approval and consent to participate

This study was carried out following the recommendations of the Animal Care and Experiment Committee of Shanghai Ninth People's Hospital, Shanghai Jiao Tong University School of Medicine. The protocol was approved by the Animal Care and Experiment Committee of Shanghai Ninth People's Hospital, Shanghai Jiao Tong University School of Medicine (SH9H-2024-A1046-SB).

## Consent for publication

Not applicable.

## Availability of data

The data generated and analyzed in this study are available from the corresponding author upon reasonable request.

## References

1. Malpartida-Carrillo V, Tinedo-Lopez PL, Guerrero ME, Amaya-Pajares SP, Özcan M, Rösing CK. Periodontal phenotype: a review of historical and current classifications evaluating different methods and characteristics. *J Esthet Restor Dent*. 2021;33(3):432-445.
doi: 10.1111/jerd.12661

2. Ramanauskaite A, Sader R. Esthetic complications in implant dentistry. *Periodontol 2000*. 2022;88(1): 73-85.
doi: 10.1111/prd.12412

3. Stefanini M, Barootchi S, Sangiorgi M, *et al*. Do soft tissue augmentation techniques provide stable and favorable peri-implant conditions in the medium and long term? A systematic review. *Clin Oral Implants Res*. 2023;34 Suppl 26:28-42.
doi: 10.1111/clr.14150

4. Thoma DS, Benić GI, Zwahlen M, Hämmerle CH, Jung RE. A systematic review assessing soft tissue augmentation techniques. *Clin Oral Implants Res*. 2009;20 Suppl 4: 146-165.
doi: 10.1111/j.1600-0501.2009.01784.x

5. Edel A. Clinical evaluation of free connective tissue grafts used to increase the width of keratinised gingiva. *J Clin Periodontol*. 1974;1(4):185-196.
doi: 10.1111/j.1600-051x.1974.tb01257.x

6. Hürzeler MB, Weng D. A single-incision technique to harvest subepithelial connective tissue grafts from the palate. *Int J Periodontics Restorative Dent*. 1999;19(3): 279-287.

7. Bertl K, Melchard M, Pandis N, Müller-Kern M, Stavropoulos A. Soft tissue substitutes in non-root coverage procedures: a systematic review and meta-analysis. *Clin Oral Investig*. 2017;21(2):505-518.
doi: 10.1007/s00784-016-2044-4

8. Song YW, Kim S, Waller T, *et al*. Soft tissue substitutes to increase gingival thickness: histologic and volumetric analyses in dogs. *J Clin Periodontol*. 2019;46(1):96-104.
doi: 10.1111/jcpe.13034

9. Valles C, Vilarrasa J, Barallat L, Pascual A, Nart J. Efficacy of soft tissue augmentation procedures on tissue thickening around dental implants: a systematic review and meta-analysis. *Clin Oral Implants Res*. 2022;33 Suppl 23:72-99.
doi: 10.1111/clr.13920

10. Montero E, Molina A, Matesanz P, Monje A, Sanz-Sánchez I, Herrera D. Efficacy of soft tissue substitutes, in comparison with autogenous grafts, in surgical procedures aiming to increase the peri-implant keratinized mucosa: a systematic review. *Clin Oral Implants Res*. 2022;33 Suppl 23:32-46.
doi: 10.1111/clr.13751

11. Rotundo R, Pancrazi GL, Grassi A, Ceresoli L, Di Domenico GL, Bonafede V. Soft tissue substitutes in periodontal and peri-implant soft tissue augmentation: a systematic review. *Materials (Basel)*. 2024;17(5)
doi: 10.3390/ma17051221

12. Alfonso García SL, Parada-Sanchez MT, Arboleda Toro D. The phenotype of gingival fibroblasts and their potential use in advanced therapies. *Eur J Cell Biol*. 2020;99(7): 151123.
doi: 10.1016/j.ejcb.2020.151123

13. Chiquet M, Katsaros C, Kletsas D. Multiple functions of gingival and mucoperiosteal fibroblasts in oral wound healing and repair. *Periodontol 2000*. 2015;68(1):21-40.
doi: 10.1111/prd.12076

14. Squier CA, Kammeyer GA. The role of connective tissue in the maintenance of epithelial differentiation in the adult. *Cell Tissue Res*. 1983;230(3):615-630.
doi: 10.1007/bf00216205

15. Hsieh PC, Jin YT, Chang CW, Huang CC, Liao SC, Yuan K. Elastin in oral connective tissue modulates the keratinization of overlying epithelium. *J Clin Periodontol*. 2010;37(8):705-711.
doi: 10.1111/j.1600-051X.2010.01542.x

16. Chuhuaicura P, Rodríguez-Niklitschek C, Oporto GH, Salazar LA. Distinct molecular mechanisms in oral mucosal wound healing: translational insights and future directions. *Int J Mol Sci*. 2025;26(21)
doi: 10.3390/ijms262110660

17. Gumede DB, Abrahamse H, Houreld NN. Targeting Wnt/β-catenin signaling and its interplay with TGF-β and Notch signaling pathways for the treatment of chronic wounds. *Cell Commun Signal*. 2024;22(1):244.
doi: 10.1186/s12964-024-01623-9

18. Das S, Jegadeesan JT, Basu B. Gelatin methacryloyl (GelMA)-based biomaterial inks: process science for 3D/4D printing and current status. *Biomacromolecules*. 2024;25(4):2156-2221.
doi: 10.1021/acs.biomac.3c01271

19. Zhang X, Huang C, Huang K, *et al*. Living and injectable porous hydrogel microspheres promoting inflammation modulation and extracellular matrix remodeling for intervertebral disc regeneration. *ACS Appl Mater Interfaces*. 2025;17(42):57953-57966.
doi: 10.1021/acsami.5c13982

20. Wei Long N, Cian V, Boyang H, Wai Yee Y, Paulo B. Advanced bioprinting strategies for fabrication of biomimetic tissues and organs. *Int J Extreme Manuf*. 2025;7(6):062006.
doi: 10.1088/2631-7990/adeee0

21. Kim JJ, Cho D-W. Advanced strategies in 3D bioprinting for vascular tissue engineering and disease modelling using smart bioinks. *Virtual Phys Prototyping*. 2024;19(1):e2395470.
doi: 10.1080/17452759.2024.2395470

22. Schwab A, Levato R, D'Este M, Piluso S, Eglin D, Malda J. Printability and shape fidelity of bioinks in 3D bioprinting. *Chem Rev*. 2020;120(19):11028-11055.
doi: 10.1021/acs.chemrev.0c00084

23. Osi AR, Zhang H, Chen J, *et al*. Three- dimensional-printable thermo/photo-cross-linked methacrylated chitosan-gelatin hydrogel composites for tissue engineering. *ACS Appl Mater Interfaces*. 2021;13(19):22902-22913.
doi: 10.1021/acsami.1c01321

24. Choi JJE, Zwirner J, Ramani RS, *et al*. Mechanical properties of human oral mucosa tissues are site dependent: a combined biomechanical, histological and ultrastructural approach. *Clin Exp Dent Res*. 2020;6(6):602-611.
doi: 10.1002/cre2.305

25. Yue K, Trujillo-de Santiago G, Alvarez MM, Tamayol A, Annabi N, Khademhosseini A. Synthesis, properties, and biomedical applications of gelatin methacryloyl (GelMA) hydrogels. *Biomaterials*. 2015;73:254-271.
doi: 10.1016/j.biomaterials.2015.08.045

26. Guan S, Zhang XL, Lin XM, Liu TQ, Ma XH, Cui ZF. Chitosan/gelatin porous scaffolds containing hyaluronic acid and heparan sulfate for neural tissue engineering. *J Biomater Sci Polym Ed*. 2013;24(8):999-1014.

doi: 10.1080/09205063.2012.731374

27. Gong H, Agustin J, Wootton D, Zhou JG. Biomimetic design and fabrication of porous chitosan–gelatin liver scaffolds with hierarchical channel network. *J Mater Sci Mater Med*. 2014;25(1):113-120.
doi: 10.1007/s10856-013-5061-8

28. Yin J, Yan M, Wang Y, Fu J, Suo H. 3D Bioprinting of low-concentration cell-laden gelatin methacrylate (GelMA) bioinks with a two-step cross-linking strategy. *ACS Appl Mater Interfaces*. 2018;10(8):6849-6857.
doi: 10.1021/acsami.7b16059

29. Peña OA, Martin P. Cellular and molecular mechanisms of skin wound healing. *Nat Rev Mol Cell Biol*. 2024;25(8):599-616.
doi: 10.1038/s41580-024-00715-1

30. Wei K, Nguyen HN, Brenner MB. Fibroblast pathology in inflammatory diseases. *J Clin Invest*. 2021;131(20).
doi: 10.1172/jci149538

31. Hu J, Li J, Jiang J, *et al*. Design of synthetic collagens that assemble into supramolecular banded fibers as a functional biomaterial testbed. *Nat Commun*. 2022;13(1):6761.
doi: 10.1038/s41467-022-34127-6

32. Mascharak S, Talbott HE, Januszyk M, *et al*. Multi-omic analysis reveals divergent molecular events in scarring and regenerative wound healing. *Cell Stem Cell*. 2022;29(2):315-327.e6.
doi: 10.1016/j.stem.2021.12.011

33. Zeng Y, Wang T, Liu Y, *et al*. Wnt and Smad signaling pathways synergistically regulated the osteogenic differentiation of fibroblasts in ankylosing spondylitis. *Tissue Cell*. 2022;77:101852.
doi: 10.1016/j.tice.2022.101852

34. Sharma S, Thakur SL, Joshi SK, Kulkarni SS. Measurement of gingival thickness using digital vernier caliper and ultrasonographic method: a comparative study. *J Investig Clin Dent*. 2014;5(2):138-143.
doi: 10.1111/jicd.12026

35. Wang J, Cha S, Zhao Q, Bai D. Methods to assess tooth gingival thickness and diagnose gingival phenotypes: a systematic review. *J Esthet Restor Dent*. 2022;34(4):620-632.
doi: 10.1111/jerd.12900

36. Heil A, Schwindling FS, Jelinek C, *et al*. Determination of the palatal masticatory mucosa thickness by dental MRI: a prospective study analysing age and gender effects. *Dentomaxillofac Radiol*. 2018;47(2):20170282.
doi: 10.1259/dmfr.20170282

37. Schwarz L, Unger E, Gahleitner A, Rausch-Fan X, Jonke E. A novel approach for gingiva thickness measurements around lower anterior teeth by means of dental magnetic resonance imaging. *Clin Oral Investig*. 2023;28(1):18.
doi: 10.1007/s00784-023-05459-4

38. Wang Z, Wang L, Li T, *et al*. 3D bioprinting in cardiac tissue engineering. *Theranostics*. 2021;11(16):7948-7969.
doi: 10.7150/thno.61621

39. Liu P, Li Q, Yang Q, *et al*. Evaluation of the effect of 3D-bioprinted gingival fibroblast-encapsulated ADM scaffolds on keratinized gingival augmentation. *J Periodontal Res*. 2023;58(3):564-574.
doi: 10.1111/jre.13126

40. Dai Y, Wang P, Mishra A, *et al*. 3D bioprinting and artificial intelligence-assisted biofabrication of personalized oral soft tissue constructs. *Adv Healthc Mater*. 2024:e2402727.
doi: 10.1002/adhm.202402727